




Cite this: *RSC Adv.*, 2018, 8, 12035

Photoluminescence properties of a $\text{ScBO}_3:\text{Cr}^{3+}$ phosphor and its applications for broadband near-infrared LEDs†

Qiyue Shao,^a *^a Hao Ding,^a Leqi Yao,^a Junfeng Xu,^b Chao Liang^b and Jianqing Jiang^c

The rapid extension of solid state lighting technologies offers the possibility to develop broadband near-infrared (NIR) phosphor-converted LEDs (pc-LEDs) as novel NIR light sources. In this paper, a new NIR-emitting phosphor $\text{ScBO}_3:\text{Cr}^{3+}$ was synthesized by a high temperature solid state reaction method. Phase structure, spectroscopic properties, luminescent lifetime, quantum yield, emitter concentration influences and thermal quenching behavior of $\text{ScBO}_3:\text{Cr}^{3+}$, as well as its applications for NIR pc-LEDs, were systematically investigated. $\text{ScBO}_3:\text{Cr}^{3+}$ phosphors exhibit a broad absorption band ranging from 400 to 530 nm, which matches well with the characteristic emission of the blue LED chip. Moreover, Cr^{3+} ions occupy the Sc^{3+} sites with relatively low crystal field strength in the ScBO_3 host, and therefore $\text{ScBO}_3:\text{Cr}^{3+}$ phosphors show intense broadband emission peaking at ~ 800 nm upon excitation at 460 nm, originating from spin-allowed ${}^4\text{T}_2 \rightarrow {}^4\text{A}_2$ transition of Cr^{3+} ions. The optimum Cr^{3+} concentration was determined to be ~ 2 mol% with a quantum yield of $\sim 65\%$. A broadband NIR pc-LED prototype device was fabricated by the combination of $\text{ScBO}_3:\text{Cr}^{3+}$ phosphors and a blue LED chip, which showed a maximum NIR light output power of ~ 26 mW and a corresponding energy conversion efficiency of $\sim 7\%$. The results indicate the great potential of $\text{ScBO}_3:\text{Cr}^{3+}$ phosphors for applications in broadband NIR pc-LEDs.

Received 3rd February 2018
 Accepted 21st March 2018

DOI: 10.1039/c8ra01084f

rsc.li/rsc-advances

Introduction

Since the first demonstration of high-brightness blue LEDs and subsequently white pc-LEDs,^{1,2} solid state lighting technologies have developed greatly and brought about a revolution in lighting and display industries. White LEDs are emerging as novel lighting sources to replace traditional incandescent and fluorescent lamps in numerous fields, due to their superior advantages including high luminous efficiency, environment friendliness, long lifetime, compactness and good reliability. The widely used method for producing white LED devices is the combination of a blue LED chip and certain phosphor materials with appropriate emission wavelengths. These white pc-LEDs possess simple device structure and low manufacturing cost. Besides white LEDs, the rapid developments of solid state lighting technologies also will provide a promising solution to

construct broadband NIR light sources, taking advantage of the phosphor-converted LED technique.^{3–7}

NIR light sources can be widely applied in a variety of fields, such as optical communication, biomedical imaging, spectroscopy, food detection, security surveillance and face (or iris) recognition.^{8–12} Incandescent bulbs, halogen lamps and AlGaAs-based LEDs are normally used as NIR light sources, however, to some extent suffering from various weaknesses. Incandescent bulbs and halogen lamps can provide continuous light emissions covering from visible to infrared ranges. However, their practical applications are limited by some drawbacks, such as large sizes, short lifetimes, low luminescent efficiency and high working temperature.⁶ In contrast, the NIR semiconductor LEDs possess small sizes, long lifetimes and high energy-conversion efficiency. Unfortunately, the LEDs normally show narrow emission bands with the largest full width at half maximum (FWHM) of ~ 40 nm,^{5,7} which are inappropriate for most spectroscopic applications. A possible solution to overcome the limitations of current NIR light sources is to design the NIR-emitting pc-LEDs, which are composed of well-established InGaN blue LED chips and NIR-emitting phosphors. The NIR pc-LEDs can benefit from the outstanding merits of the blue-emitting InGaAl LED chips, such as relatively higher thermal stability, continuously increased luminous efficiency and decreased manufacturing cost. Since the invention of high-brightness blue LEDs in the mid 1990s,^{1,2} steady

^aSchool of Materials Science and Engineering, Jiangsu Key Laboratory for Advanced Metallic Materials, Southeast University, Nanjing 211189, PR China. E-mail: qiyueshao@seu.edu.cn

^bJiangsu Bree Optronics Co., Ltd., Nanjing 211103, PR China

^cSchool of Materials Science and Engineering, Nanjing Forestry University, Nanjing 210037, PR China

† Electronic supplementary information (ESI) available. See DOI: 10.1039/c8ra01084f



improvements have been achieved for InGaN-based blue LEDs. According to Haitz's law, the light output per LED package increases by a factor of twenty every decade, and the cost per lumen falls by a factor of ten.¹³ On the other hand, broadband and wavelength-tunable emissions can be expected for NIR pc-LEDs through the rational selection of emitting ions and host materials of NIR-emitting phosphors. Moreover, the continuous emission spectra will be achieved by the appropriate combination between various types of phosphor materials that possess various emission wavelengths upon excitation by the blue light.

To design NIR-emitting phosphors excited by the blue light, the emitting ions should be first of all chosen reasonably. The utilization of 4f–4f transitions of trivalent lanthanide ions is hampered by their spectrally narrow and low intensity absorption.^{3,4} For divalent or trivalent lanthanide ions (e.g., Eu²⁺ and Ce³⁺) featuring 4f–5d optical transitions, it is difficult to achieve the light emissions in the NIR spectral range due to the large energy separation between 4f and 5d levels. Recently, Bi-doped crystals and glasses have attracted intense attention due to their super broadband emissions from visible to NIR.^{14–16} However, the luminescent behaviour of Bi-active centre has not been well understood, and it is still a big challenge to improve its NIR emission efficiency.⁶ Transition metal ions with incomplete 3d shells (3dⁿ, n < 10) have a number of low-lying energy states, between which radiative transitions in the NIR spectral region may occur. Moreover, because they are strongly coupled to the coordination ligands in hosts, optical transitions of transition metal ions are significantly affected by the crystal field symmetry and strength. In general, transition metal ions show relatively strong and broad excitation bands, as well as wavelength-tunable broadband emissions. As typical transition metal ions, Cr³⁺ ions in the material ruby (Al₂O₃:Cr³⁺) have been thoroughly investigated by spectroscopists for over a hundred years.¹⁷ Laser-related spectroscopy of Cr³⁺ ions in a variety of crystals has also been extensively studied for the developments of tunable solid state lasers.¹⁸ Recently, NIR long-persistent luminescence of Cr³⁺-activated gallate phosphors has gained considerable attention due to their potential applications in optical information storage, night-vision surveillance and bio-imaging.^{19–23} Cr³⁺ ions exhibit strong absorption band in the visible spectral range and can be effectively excited by the blue light. In addition, in contrast to sharp emission lines arising from the ²E → ⁴A₂ transition of Cr³⁺ ions in strong-field sites (e.g., Al₂O₃:Cr³⁺), a tunable broad emission band arising from the ⁴T₂ → ⁴A₂ transition can be observed when Cr³⁺ ions occupy lattice sites with relatively weak crystal field.^{17,24} These optical characteristics imply that Cr³⁺ ions are an ideal choice of luminescence centres for the development of novel NIR-emitting phosphors.

In this paper, NIR-emitting ScBO₃:Cr³⁺ phosphors were synthesized *via* solid state reaction, and their crystal structure, photoluminescence (PL) and thermal quenching properties were systemically investigated. Cr³⁺-doped ScBO₃ single crystals have been considered as room temperature near-infrared tunable laser materials by Lai *et al.* in the mid 1980s.²⁵ However, structural and spectroscopic characteristics of ScBO₃:Cr³⁺ phosphors are far from systematic studies and

especially its applicability for NIR pc-LEDs deserve further investigations. In this work, a prototype of the NIR pc-LED was also fabricated on the basis of the ScBO₃:Cr³⁺ phosphors and a blue LED chip, and its electroluminescence properties were studied. The results demonstrate the great potential of ScBO₃:Cr³⁺ phosphors for applications in broadband NIR-emitting pc-LEDs.

Experimental section

Phosphor synthesis

Sc_{1-x}Cr_xBO₃ (x = 0.005–0.1) phosphors were synthesized *via* a solid state reaction method. Sc₂O₃ (99.99%), H₃BO₃ (99.95%) and Cr₂O₃ (99.95%) were used as starting materials. Stoichiometric amounts of raw materials were weighed and thoroughly mixed, except that 25% excess of H₃BO₃ was added to compensate its evaporation loss in course of high temperature sintering. Subsequently, the powder mixture was transferred into an alumina crucible and calcined in a muffle furnace at 1300 °C for 10 h. Finally, the as-prepared products were naturally cooled down to room temperature and ground to fine powders for subsequent characterization.

Phosphor characterization

The phase structure of phosphors was identified by powder X-ray diffraction (XRD) measurements on a D8 Discover diffractometer (Bruker) with Cu K α radiation ($\lambda = 1.5406 \text{ \AA}$). Rietveld structure refinements were conducted using the general structure analysis system (GSAS) program.²⁶ The particle morphology was observed on a Sirion field-emission scanning electron microscope (FE-SEM, FEI). Diffuse reflection spectrum measurements were performed on a Cary 5000 UV-vis-NIR spectrophotometer (Varian) equipped with an internal diffuse reflectance accessory. The PL excitation spectra were measured on an F-7000 fluorescence spectrophotometer (Hitachi). The PL emission spectra were obtained on a Maya2000 portable spectrometer (Ocean Optics) using a blue LED ($\lambda_{\text{em}} = 450 \text{ nm}$) as the excitation source. Temperature-dependent (30–250 °C) emission spectra were measured with the assistance of a self-designed heating system. The luminescent decay curves were measured by a FluoroMax-4 fluorescence spectrometer (Horiba Jobin Yvon). The quantum yield (QY) was measured by an integrating sphere equipped with a Maya2000 spectrometer and a blue LED, and the spectrometer was carefully calibrated by a standard tungsten lamp. The quantum yield is defined as the percentage of the number of emitted photons to that of absorbed photons, which can be calculated using the following equation:²⁷

$$\eta = \frac{L_{\text{sample}}}{E_{\text{reference}} - E_{\text{sample}}} \times 100\% \quad (1)$$

where η is the quantum yield, L_{sample} is the integrated emission intensity of the sample, whereas $E_{\text{reference}}$ and E_{sample} represent the integrated intensities of the excitation light with and without the sample in the integrating sphere, respectively.



NIR pc-LED fabrication and performance measurement

NIR pc-LEDs were fabricated by applying a mixture of ScBO_3 - Cr^{3+} phosphors and transparent silicon resin on an InGaN blue LED chip ($\lambda_{\text{em}} = 455 \text{ nm}$). Photographs of the lighted pc-LED were taken by a cellphone's camera (Samsung S7), which used a Si-based photodetector covering the spectral range up to $\sim 1100 \text{ nm}$. When taking the picture, an 800 nm long-pass filter was used to remove all the visible light. For electroluminescence (EL) measurements, the packaged LED device was operated at a DC forward bias of $\sim 3.0 \text{ V}$ with various injection currents, and the EL spectral distribution was recorded using an integrating sphere and a corrected Maya2000 spectrometer. The NIR light output power of the pc-LED was measured by a FieldMate light power meter (Coherent) equipped a PM10 thermopile sensor, where a 600 nm long-pass filter was used to remove the residual blue light from the LED chip. The energy conversion efficiency was defined as the ratio of the NIR light output power to the input electrical power.

Results and discussion

Structural analysis

Rietveld structure refinements of as-prepared ScBO_3 and $\text{ScBO}_3:0.02\text{Cr}^{3+}$ samples were performed to identify their phase structure. The crystallographic data (ICSD# 65010) reported by Keszler *et al.* was adopted as the initial model.²⁸ Fig. 1 shows the refined XRD patterns of ScBO_3 and $\text{ScBO}_3:0.02\text{Cr}^{3+}$, and the final refinement parameters are listed in Table 1. The refined profiles confirm the phase purity without unidentified diffraction peaks from impurity, regardless of Cr^{3+} doping. Both ScBO_3 and $\text{ScBO}_3:\text{Cr}^{3+}$ are found to crystallize as a rhombohedral structure with a space group of $R\bar{3}c$ (no. 167). Fig. 2 displays the crystal cell of ScBO_3 and the coordination environment of $[\text{ScO}_6]$ group. In ScBO_3 , Sc^{3+} ions are coordinated by six oxygen atoms and B^{3+} ions are surrounded by three oxygen atoms. ScBO_3 exhibits a layered calcite-like structure, which is composed of $[\text{ScO}_6]$ octahedron and trigonal planar $[\text{BO}_3]$ group. Structural connectivity between the $[\text{ScO}_6]$ and $[\text{BO}_3]$ group occurs only *via* corner-sharing.

For the ScBO_3 host, the lattice parameters are calculated to be $a = b = 4.7516(5) \text{ \AA}$, $c = 15.2835(7) \text{ \AA}$, $V = 298.84(1) \text{ \AA}^3$, and $Z = 6$. For $\text{ScBO}_3:0.02\text{Cr}^{3+}$, the smaller lattice parameters are determined: $a = b = 4.7481(9) \text{ \AA}$, $c = 15.2641(1) \text{ \AA}$, $V = 298.03(1) \text{ \AA}^3$. The effective ionic radius of Cr^{3+} is 0.615 \AA when the coordination number (CN) is equal to 6, which is close to that of Sc^{3+} (0.745 \AA , CN = 6) and far larger than that of B^{3+} (0.27 \AA , CN = 6).²⁹ Therefore, Cr^{3+} ions prefer to occupy the Sc^{3+} sites with octahedral coordination in $\text{ScBO}_3:\text{Cr}^{3+}$ phosphors. Due to the smaller ionic radius of Cr^{3+} , the calculated cell parameters and Sc–O bond length of $\text{ScBO}_3:0.02\text{Cr}^{3+}$ are slightly smaller than that of pure ScBO_3 (Table 1).

XRD patterns of $\text{ScBO}_3:\text{Cr}^{3+}$ phosphors with various Cr^{3+} concentrations are shown in Fig. 3a. All the diffraction peaks of $\text{ScBO}_3:x\text{Cr}^{3+}$ ($x = 0.01\text{--}0.08$) phosphors agree well with those of a rhombohedral ScBO_3 structure (JCPDS Card no. 79-0097). No

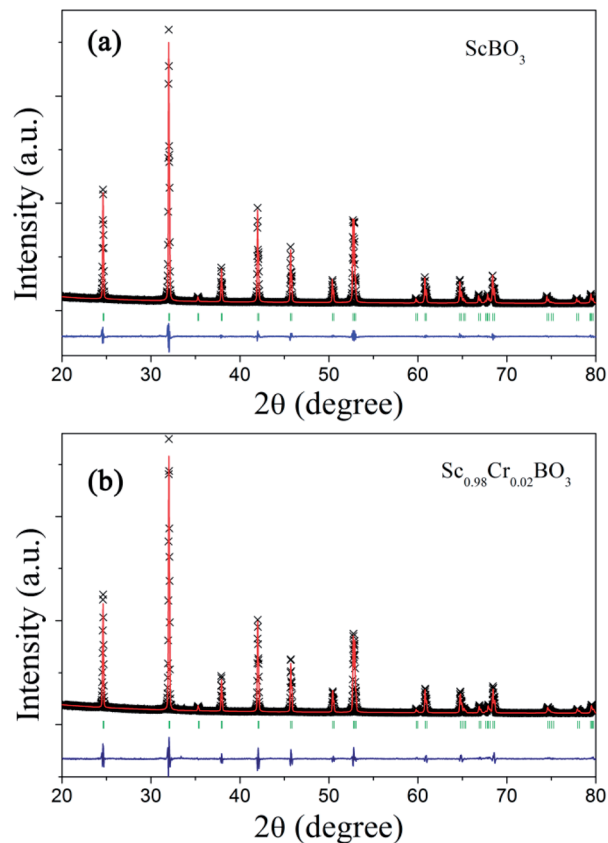


Fig. 1 Experimental (cross), calculated (solid line), Bragg positions (tick mark) and differences (bottom) results of powder XRD refinements of (a) ScBO_3 and (b) $\text{ScBO}_3:0.02\text{Cr}^{3+}$.

impurity phase can be recognized with the increase of Cr^{3+} contents.

Noting that the XRD peaks of $\text{ScBO}_3:x\text{Cr}^{3+}$ phosphors shift to higher diffraction angle with increasing the Cr^{3+} concentration

Table 1 Rietveld structure refinements and lattice parameters for ScBO_3 and $\text{ScBO}_3:0.02\text{Cr}^{3+}$

	ScBO_3	$\text{ScBO}_3:0.02\text{Cr}^{3+}$
Space group	$R\bar{3}c$	
Symmetry	Rhombohedral	
Cell parameters		
$a = b$ (Å)	4.7516(5)	4.7481(9)
c (Å)	15.2835(7)	15.2641(1)
$\alpha = \beta, \gamma$ (°)	90°, 120°	90°, 120°
Z , volume (Å ³)	6, 298.84(1)	6, 298.03(1)
R_p (%), R_{wp} (%)	6.43%, 8.57%	8.45%, 11.51%
χ^2	3.163	6.672
Bond distance and angle		
B–O (Å)	1.37624(1)	1.3916(18)
Sc–O (Å)	2.12198(2)	2.1124(9)
$\angle \text{OBO}$ (°)	120	120
$\angle \text{OScO}$ (°)	87.686(1), 180.000(0), 92.314(1)	87.483(25), 180.000(0), 92.517(25)



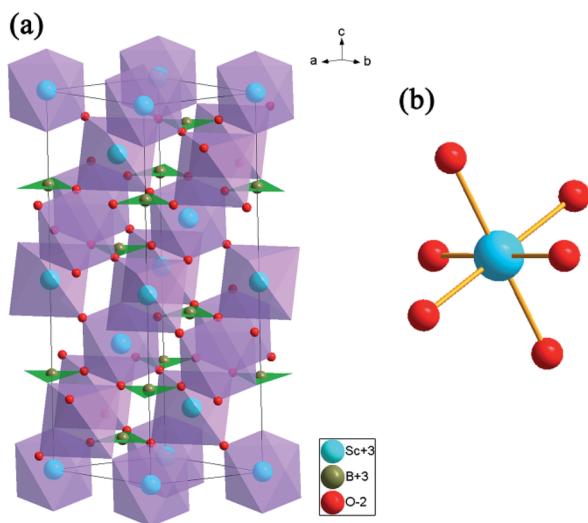


Fig. 2 (a) The crystal structure representation of ScBO_3 and (b) the coordination environment of $[\text{ScO}_6]$ octahedron.

(Fig. 3b), indicative of the decrease of lattice interplanar spacing due to the smaller ionic radius of Cr^{3+} . The SEM image (Fig. 3c) shows that the obtained $\text{ScBO}_3:\text{Cr}^{3+}$ phosphor is mainly composed of a large number of spherical particles with an average size of 1–3 μm , except that a few large-sized particles (>5 μm) are also observed.

Spectroscopic properties

When Cr^{3+} ($3d^3$) ions occupy lattice sites with octahedral coordination, their energy level distribution can be illustrated by

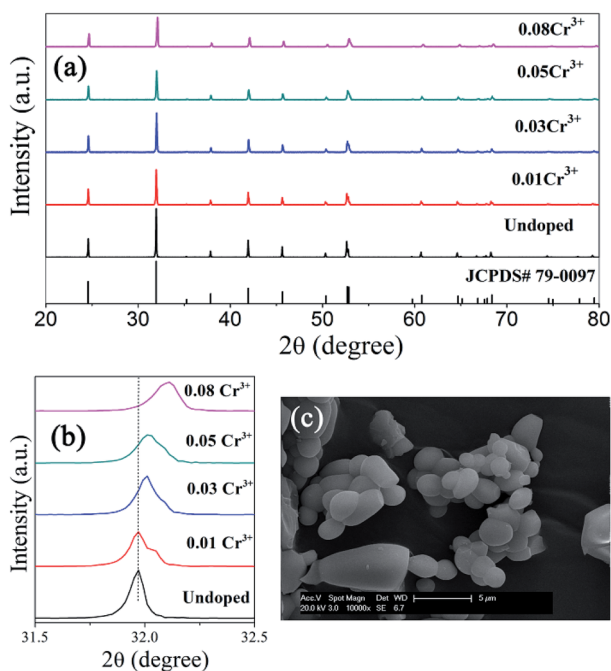


Fig. 3 (a) XRD patterns of $\text{ScBO}_3:\text{xCr}^{3+}$ phosphors with various x values, together with the standard pattern of a rhombohedral ScBO_3 structure (JCPDS Card no. 79-0097) for comparison; (b) magnified XRD peak at $\sim 32^\circ$; (c) SEM image of $\text{ScBO}_3:0.02\text{Cr}^{3+}$ (scale bar: 5 μm).

Tanabe–Sugano diagram (Fig. 4a).³⁰ Except for ${}^2\text{E}$ and ${}^2\text{T}_1$ levels, most of Cr^{3+} crystal field levels (e.g., ${}^4\text{T}_2$, ${}^4\text{T}_1$, ${}^2\text{A}_1$) show strong dependences on Dq/B values, where Dq and B are the crystal field strength and Racah parameters, respectively.^{17,31} Optical transitions of Cr^{3+} ions can be understood in more detail with the aid of their configuration coordinate diagrams (Fig. 4b). Noting that ${}^4\text{A}_2$ and ${}^2\text{E}$ states are derived from the t_3 2 crystal field orbital, whereas ${}^4\text{T}_2$ and ${}^4\text{T}_1$ states are originated from the t_2 2e orbital.^{17,32} Accordingly, there is a small shift in equilibrium distance between the parabolas of ${}^4\text{A}_2$ and ${}^2\text{E}$ states in configuration coordinate diagram. In contrast, the parabolas of ${}^4\text{T}_2$ and ${}^4\text{T}_1$ states exhibit a larger offset compared to that of the ground state ${}^4\text{A}_2$. The absorption spectra of Cr^{3+} -doped compounds are normally characterized by two broad absorption bands in the visible spectral range, arising from the spin-allowed ${}^4\text{A}_2 \rightarrow {}^4\text{T}_2$ and ${}^4\text{A}_2 \rightarrow {}^4\text{T}_1$ transitions, respectively. The emission band shapes of Cr^{3+} ions are determined by the host crystal field strength, depending on the fact whether the ${}^2\text{E}$ or ${}^4\text{T}_2$ level is lowest. As shown in Fig. 4a, ${}^2\text{E}$ and ${}^4\text{T}_2$ levels cross at $Dq/B \approx 2.3$.¹⁷ When Cr^{3+} ions occupy high-field sites ($Dq/B > 2.3$), ${}^2\text{E}$ will be the emitting state and the Cr^{3+} emission spectra is characterized by sharp emission lines (${}^2\text{E} \rightarrow {}^4\text{A}_2$). When Cr^{3+} ions occupy low-field sites ($Dq/B < 2.3$), the ${}^4\text{T}_2 \rightarrow {}^4\text{A}_2$ transition will dominate the Cr^{3+} luminescence featuring a very broad emission band (Fig. 4b).

Fig. 5a shows the diffuse reflection spectra of ScBO_3 and $\text{ScBO}_3:\text{xCr}^{3+}$ samples. Two broad absorption bands centred at ~ 460 and 645 nm were detected after the incorporation of Cr^{3+} ions into the ScBO_3 host, which are originated from the ${}^4\text{A}_2 \rightarrow {}^4\text{T}_1$ and ${}^4\text{A}_2 \rightarrow {}^4\text{T}_2$ transitions of Cr^{3+} ions (Fig. 4b), respectively. With the increase of Cr^{3+} contents, a continuous enhancement in absorptivity can be found. Fig. 5b represents the excitation and emission spectra of $\text{ScBO}_3:0.02\text{Cr}^{3+}$ phosphors. Upon excitation at 450 nm, the PL spectrum displays a broad emission band extending from 700 to 950 nm, with a maximum at ~ 800 nm and a FWHM value of ~ 120 nm. The broad emission band should be attributed to the spin-allowed

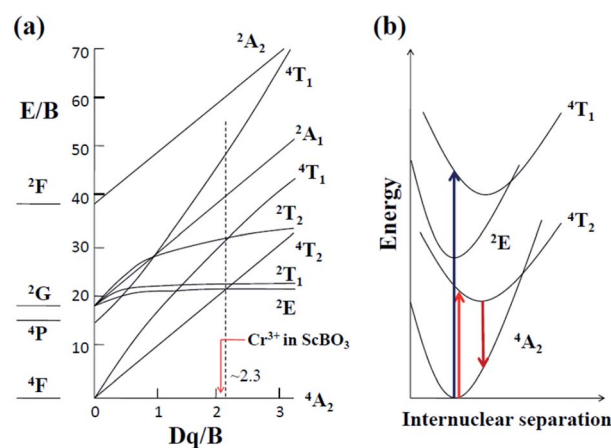


Fig. 4 (a) Tanabe–Sugano energy level diagram for Cr^{3+} ($3d^3$) ions in an octahedral crystal field (Dq : the octahedral crystal field parameter, B : Racah parameter); (b) configurational coordinate diagram of Cr^{3+} ions in a weak crystal field, e.g. in the ScBO_3 host.



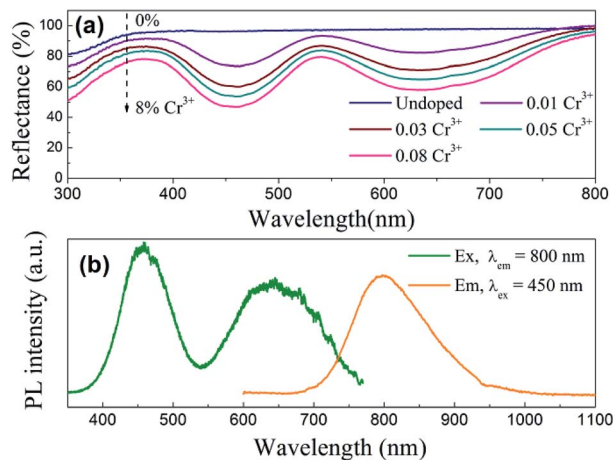


Fig. 5 (a) Diffuse reflection spectra of ScBO_3 and $\text{ScBO}_3:x\text{Cr}^{3+}$; (b) excitation and emission spectra of $\text{ScBO}_3:0.02\text{Cr}^{3+}$ phosphors.

${}^4\text{T}_2 \rightarrow {}^4\text{A}_2$ transition of Cr^{3+} ions (Fig. 4b). The excitation spectrum monitored at ~ 800 nm is composed of two excitation bands at ~ 460 and 645 nm, which is consistent with the diffuse reflection spectra of $\text{ScBO}_3:\text{Cr}^{3+}$ phosphors.

For pc-LED applications, the quantum yield (QY) of the phosphors is an important factor that should be considered. The quantitative excitation profiles and emission spectra of the $\text{ScBO}_3:0.02\text{Cr}^{3+}$ phosphor and the reference sample were recorded upon excitation at ~ 450 nm using an integrating sphere (Fig. S1†). According to eqn (1), the quantum yield of the $\text{ScBO}_3:0.02\text{Cr}^{3+}$ phosphor is calculated to be $\sim 65\%$ under 450 nm excitation. The ~ 460 nm excitation band of $\text{ScBO}_3:\text{Cr}^{3+}$ phosphors matches well the emissions of the blue LED chips. In combination with their broadband emission at ~ 800 nm, $\text{ScBO}_3:\text{Cr}^{3+}$ phosphors show great potential for applications in NIR pc-LED devices based on the blue LED chip.

The Stokes shift with respect to the transition between ${}^4\text{A}_2$ and ${}^4\text{T}_2$ levels is determined to be ~ 3004 cm^{-1} by the comparison between the corresponding spectral positions of room-temperature excitation (~ 15504 cm^{-1}) and emission (~ 12500 cm^{-1}) bands. From the spectral positions of ${}^4\text{A}_2 \rightarrow {}^4\text{T}_2$ and ${}^4\text{A}_2 \rightarrow {}^4\text{T}_1$ excitation bands shown in Fig. 5b, the values of the crystal field Dq and Racah B parameters can be calculated using the following equations:^{17,33}

$$E({}^4\text{T}_2) = 10Dq \quad (2)$$

$$\frac{Dq}{B} = \frac{15(\Delta E/Dq - 8)}{(\Delta E/Dq)^2 - 10(\Delta E/Dq)} \quad (3)$$

where ΔE is the energy separation between ${}^4\text{T}_2$ and ${}^4\text{T}_1$ states. The value of ΔE is determined by the direct comparison between the spectral positions of ${}^4\text{A}_2 \rightarrow {}^4\text{T}_2$ and ${}^4\text{A}_2 \rightarrow {}^4\text{T}_1$ excitation bands. The energy value (E) of the ${}^4\text{T}_2$ level is determined from the excitation peak of the ${}^4\text{A}_2 \rightarrow {}^4\text{T}_2$ transition, at the same time taking into account the influences of the Stokes shift.³¹ Herein, the difference in force constants between the ${}^4\text{A}_2$ and ${}^4\text{T}_2$ (or ${}^4\text{T}_1$) parabolas is approximately ignored (Fig. 4b). The values of Dq and B are calculated to be ~ 1400 and 651 cm^{-1} , respectively.

The Dq/B value is about 2.15, which is lower than 2.3, indicating that Cr^{3+} ions occupy lattice sites in ScBO_3 with lower crystal field strength (Fig. 4a). Based on structural analysis, Cr^{3+} ions preferentially occupy the Sc^{3+} sites in $\text{ScBO}_3:\text{Cr}^{3+}$ phosphors. The weak crystal field should be related to longer Sc–O bond distance in ScBO_3 , because the crystal field strength is inversely proportional to the distance between the central ions and coordination ions.³¹

Cr^{3+} concentration effects

Fig. 6a shows the PL emission spectra of $\text{ScBO}_3:x\text{Cr}^{3+}$ phosphors with various Cr^{3+} contents. The spectral profile changes little with the increase of Cr^{3+} concentrations. The peak wavelengths of broad emission bands of $\text{ScBO}_3:x\text{Cr}^{3+}$ phosphors exhibit a slight red-shift with increasing x values (Fig. S2†), despite the fact that the Sc–O distance decreases at higher Cr^{3+} contents. We believe the re-absorption between activator ions play an important role in $\text{ScBO}_3:x\text{Cr}^{3+}$ phosphor with larger x values. As shown in Fig. 5b, the long-wavelength excitation band of $\text{ScBO}_3:\text{Cr}^{3+}$ slightly overlaps with the emission band, and the re-absorption between Cr^{3+} ions will reduce the emission at the blue wing and result in the red-shift of emission band.

The emission intensities of $\text{ScBO}_3:x\text{Cr}^{3+}$ phosphors increase with increasing x values and reach a maximum at a critical concentration of $x = 0.02$. A further increase in the Cr^{3+} concentration results in the decrease of the emission intensity due to the concentration quenching effect (Fig. 6b). Nonradiative

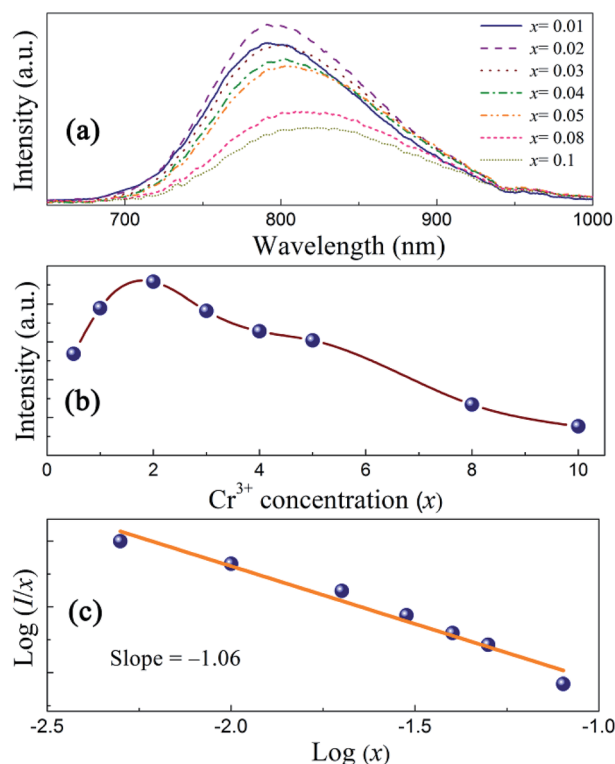


Fig. 6 (a) Emission spectra, (b) plots of I vs. x and (c) $\log(I/x)$ vs. $\log(x)$ of $\text{ScBO}_3:x\text{Cr}^{3+}$ phosphors ($\lambda_{\text{ex}} = 450$ nm) with various Cr^{3+} contents.



energy migration among luminescence centres can occur *via* exchange interaction or multipole–multipole interaction. In this case, the critical energy transfer distance (R_c) can be approximately estimated by the following equation proposed by Blasse:³¹

$$R_c \approx 2 \left(\frac{3V}{4\pi x_c N} \right)^{1/3} \quad (4)$$

where V is the unit cell volume, x_c is the critical activator concentration and N is the number of the total activator sites per unit cell. For $\text{ScBO}_3:0.02\text{Cr}^{3+}$, $V = 298.03 \text{ \AA}^3$, $x_c = 0.02$, $N = 6$, and therefore the R_c value is determined to be $\sim 16.8 \text{ \AA}$. The exchange interaction is a short-range effect and usually takes effect only when the distance between activators is shorter than 5 \AA . Therefore, nonradiative electric multipolar interaction is the preferred energy transfer mechanism between Cr^{3+} ions in ScBO_3 . In this case, the luminescent intensity per activator can be expressed by the following equation:³⁴

$$\frac{I}{x} = \frac{k}{1 + \beta(x)^{\theta/3}} \quad (5)$$

where I is the PL intensity, k and β are constants depending on the interaction type and the host lattice, and x represents the Cr^{3+} doping concentration. According to the research work of Van Uitert,³⁴ $\theta = 3$ corresponds to the energy transfer among the nearest-neighbor ions, whereas $\theta = 6, 8$, and 10 correspond to the dipole–dipole, dipole–quadrupole, and quadrupole–quadrupole interactions, respectively. As shown in Fig. 6c, the correlation between $\log(I/x)$ and $\log(x)$ can be fitted linearly and the slope ($\theta/3$) is determined to be -1.06 . The calculated θ value is close to 3, implying that the quenching tends to be proportional to the activator concentration and the concentration quenching mechanism of $\text{ScBO}_3:x\text{Cr}^{3+}$ phosphors can be attributed to the nonradiative energy transfer among the nearest-neighbor ions.^{34–36}

Fig. 7 shows the luminescent decay curves of $\text{ScBO}_3:x\text{Cr}^{3+}$ phosphors with various x values. All the decay curves can be well fitted by a single exponential function (Fig. S3†). The luminescent lifetime (τ) are determined to approximately

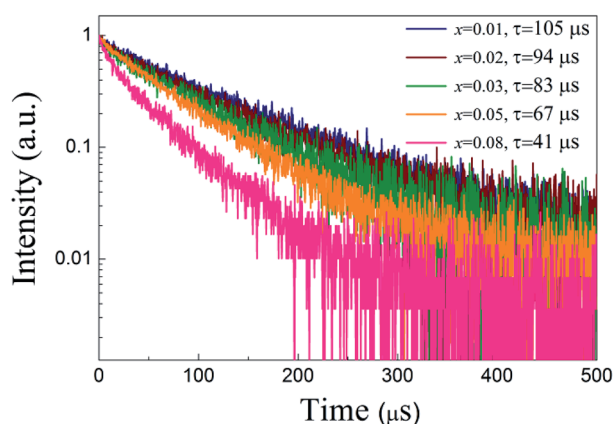


Fig. 7 Luminescent decay curves of $\text{ScBO}_3:x\text{Cr}^{3+}$ phosphors with various Cr^{3+} concentrations ($\lambda_{\text{ex}} = 450 \text{ nm}$).

105, 94, 83, 67 and $41 \mu\text{s}$ for $\text{ScBO}_3:x\text{Cr}^{3+}$ where $x = 0.01, 0.02, 0.03, 0.05, 0.08$. The decrease of the Cr^{3+} lifetime is attributed to the increased luminescent quenching effect at higher Cr^{3+} concentrations. The well fitting results of luminescent decay curves by a single exponential function also indicate that the Cr^{3+} ions occupy only single lattice site in the ScBO_3 host.

Temperature-dependent PL properties

Luminescent thermal stability is another important factor of the phosphors for pc-LED applications. It is well known that the emission intensity of luminescent materials usually decreases in different degrees at elevated temperatures due to increased nonradiative transitions. The working temperature of LED devices can be higher than $100 \text{ }^\circ\text{C}$,³⁷ and therefore the phosphor materials should maintain their luminescent intensity at higher temperatures for pc-LED applications. Fig. 8a represents the PL spectra of $\text{ScBO}_3:0.02\text{Cr}^{3+}$ at various temperatures ($30\text{--}250 \text{ }^\circ\text{C}$), where a thermal quenching behaviour can be observed. With the temperature increasing from 30 to $150 \text{ }^\circ\text{C}$, the emission intensity of $\text{ScBO}_3:0.02\text{Cr}^{3+}$ decreases by approximately 51% from the initial intensity (Fig. 8b). NIR-emitting $\text{ScBO}_3:\text{Cr}^{3+}$ phosphors show lower thermal stability than the commercial

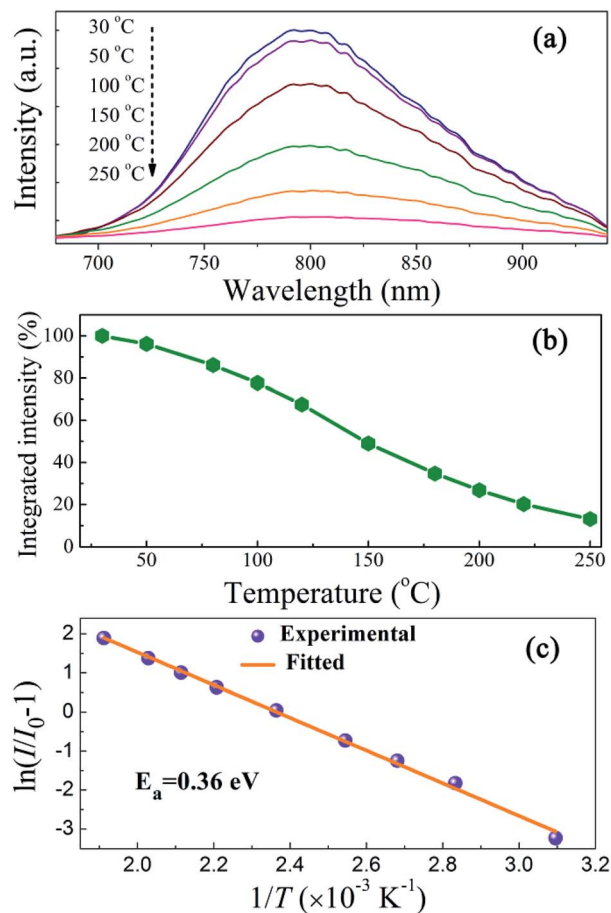


Fig. 8 (a) Temperature-dependent emission spectra, (b) temperature-dependent normalized integrated intensities and (c) activation energy plots using the modified Arrhenius equation for $\text{ScBO}_3:0.02\text{Cr}^{3+}$ phosphors ($\lambda_{\text{ex}} = 450 \text{ nm}$).



visible-emitting phosphors, such as $\text{Y}_3\text{Al}_5\text{O}_{12}:\text{Ce}^{3+}$ and $\text{CaAlSiN}_3:\text{Eu}^{2+}$, for which larger than 80% of the emission intensity at room temperature can be retained at 150 °C.^{38,39} The thermal quenching of $\text{ScBO}_3:\text{Cr}^{3+}$ can be caused *via* two possible routes:³¹ (1) multi-phonon emission directly across the energy gap between the excited state $^4\text{T}_2$ and the ground state $^4\text{A}_2$; (2) nonradiative transition through the crossing of $^4\text{T}_2$ and $^4\text{A}_2$ parabolas (Fig. 4b). The increased thermal quenching of $\text{ScBO}_3:\text{Cr}^{3+}$ is probably related to the narrow energy gap between $^4\text{T}_2$ and $^4\text{A}_2$ levels, as well as the larger Stokes shift of the phosphor.

The temperature-dependence of the emission intensity can be described by a modified Arrhenius equation:⁴⁰

$$I(T) = \frac{I_0}{1 + A \exp(-E_a/kT)} \quad (6)$$

where I_0 is the initial intensity, $I(T)$ is the intensity at a given temperature, A is a constant, k is the Boltzmann constant and E_a is the activation energy for the thermal quenching. Fig. 8c depicts a plot of $\ln(I/I_0 - 1)$ versus $1/T$, and the activation energy (E_a) is determined to be ~ 0.36 eV for $\text{ScBO}_3:\text{Cr}^{3+}$ phosphors through the best fit of the Arrhenius equation.

Fabrication and performance of NIR pc-LED

In order to demonstrate the applicability of $\text{ScBO}_3:\text{Cr}^{3+}$ phosphors, a NIR pc-LED prototype was fabricated by the combination of a 455 nm InGaN LED chip and the $\text{ScBO}_3:0.02\text{Cr}^{3+}$ phosphor. Photographs of the as-fabricated pc-LED device and the lighted one are shown in the insets of Fig. 9a. Bright NIR emission could be photographed by a cellphone's camera after the visible light was removed by an 800 nm long-pass filter. Fig. 9a shows a downshift on the emission that called here electroluminescence (EL) spectrum, even if there is no direct electron-excitation of the as-fabricated pc-LED at various drive currents. The blue emission band at ~ 455 nm comes from the LED chip and the broad emission band between 700–950 nm is attributed to $\text{ScBO}_3:\text{Cr}^{3+}$ phosphors. With the increase in the drive current at a forward bias of ~ 3 V, no obvious changes in the EL profile can be found, except for the continuous increase of the luminescence intensity.

Fig. 9b represents the dependences of the NIR light output on the injection current of the pc-LED device. A continuous increase in the NIR light output power is found with increasing the injection current. A maximum output power of ~ 26 mW is achieved at a drive current of 120 mA. The energy conversion efficiency is calculated to be approximately 7%, much larger than the reported values of NIR pc-LEDs based on trivalent lanthanide doped glass phosphors.^{3,4} Noting that the energy conversion efficiency of the LED chip used here is about 20% and the blue light from the LED chip still remains for the NIR pc-LED device. The energy conversion efficiency can be further improved by engineering the package structure and utilizing more efficient blue LED chips. These results demonstrate the great potential of $\text{ScBO}_3:\text{Cr}^{3+}$ phosphors as an alternative NIR component for applications in broadband NIR pc-LEDs.

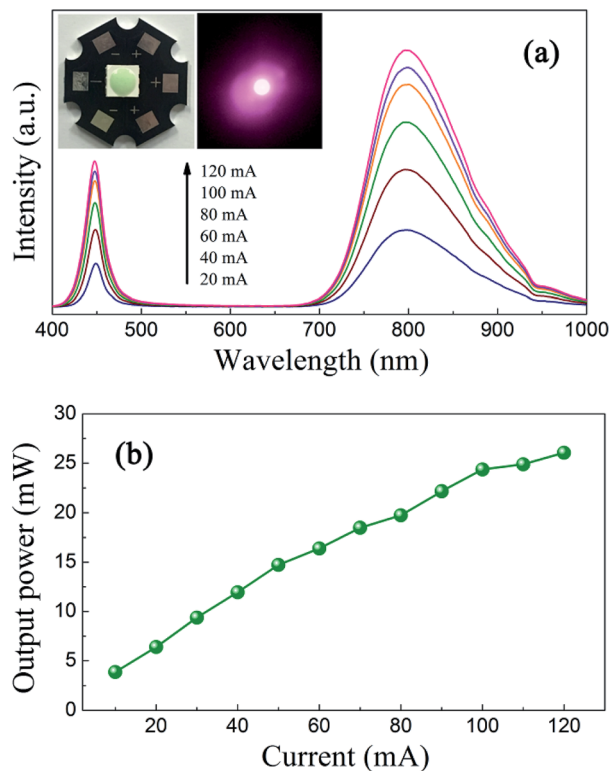


Fig. 9 (a) Electroluminescence spectra of the pc-LED under various drive currents. The insets give photographs of the as-fabricated pc-LED and the lighted one in pseudo color. (b) The NIR light output power as a function of the drive current.

Conclusions

$\text{ScBO}_3:\text{Cr}^{3+}$ phosphors were synthesized *via* a solid state reaction method and investigated for their structural and luminescent characteristics. The phase structure of as-prepared phosphors was confirmed by the Rietveld analysis. In the ScBO_3 host, Cr^{3+} ions preferentially occupied Sc^{3+} sites with low-field octahedral coordination. Therefore, a broadband emission ($\lambda_{\text{max}} = \sim 800$ nm) in the NIR spectral range between 700–950 nm was observed for $\text{ScBO}_3:\text{Cr}^{3+}$ upon excitation by the blue light, which was attributed to $^4\text{T}_2 \rightarrow ^4\text{A}_2$ transitions of Cr^{3+} ions. The luminescent quenching was proportional to the Cr^{3+} concentration in $\text{Sc}_{1-x}\text{Cr}_x\text{BO}_3$ phosphors, and the maximum emission intensity was found at $x = 0.02$ with a quantum yield of $\sim 65\%$. The thermal quenching properties of $\text{ScBO}_3:\text{Cr}^{3+}$ phosphors were also inspected and the activation energy was determined to be ~ 0.36 eV. By integrating $\text{ScBO}_3:\text{Cr}^{3+}$ phosphors on the blue LED chip, a broadband NIR pc-LED was obtained with a maximum NIR light output of ~ 26 mW and the corresponding energy conversion efficiency of $\sim 7\%$. The results suggest that $\text{ScBO}_3:\text{Cr}^{3+}$ phosphors can potentially serve as conversion phosphors for broadband NIR pc-LED devices.

Conflicts of interest

There are no conflicts to declare.



Acknowledgements

This work was supported by the Natural Science Foundation of Jiangsu Province of China (BK20160073) and the Jiangsu Key R&D Program (BE2015102).

Notes and references

- 1 S. Nakamura, T. Mukai and M. Senoh, *Appl. Phys. Lett.*, 1994, **64**, 1687–1689.
- 2 S. Nakamura and G. Fasol, *The blue laser diode, GaN based light emitters and lasers*, Springer, Berlin, 1997.
- 3 K. Oshima, K. Terasawa, S. Fuchi and Y. Takeda, *Phys. Status Solidi C*, 2012, **9**, 2340–2343.
- 4 S. Fuchi, Y. Shimizu, K. Watanabe, H. Uemura and Y. Takeda, *Appl. Phys. Express*, 2014, **7**, 072601.
- 5 S. Möller, A. Katelnikovas, M. Haase and T. Jüstel, *J. Lumin.*, 2016, **172**, 185–190.
- 6 D. Hayashi, A. M. Van Dongen, J. Boerekamp, S. Spoor, G. Lucassen and J. Schleipen, *Appl. Phys. Lett.*, 2017, **110**, 233701.
- 7 B. Malysaa, A. Meijerink, W. W. Wu and T. Jüstel, *J. Lumin.*, 2017, **190**, 234–241.
- 8 H. Y. Zhu, S. O. Isikman, O. Mudanyali, A. Greenbaum and A. Ozcan, *Lab Chip*, 2013, **13**, 51–67.
- 9 P. A. Martina, *Chem. Soc. Rev.*, 2002, **31**, 201–210.
- 10 L. S. Magwaza, U. L. Opara, H. Nieuwoudt, P. J. R. Cronje, W. Saeys and B. Nicolaï, *Food Bioprocess Technol.*, 2012, **5**, 425–444.
- 11 N. Salamati, Z. Sadeghipoor and S. Süsstrunk, *Proc. SPIE*, 2011, **7865**, 786508.
- 12 J. Dowdall, I. Pavlidis and G. Bebis, *Image Vis. Comput.*, 2003, **21**, 565–578.
- 13 R. Haitz and J. Y. Tsao, *Phys. Status Solidi A*, 2011, **208**, 17–29.
- 14 J. Y. Zheng, L. L. Tan, L. P. Wang, M. Y. Peng and S. H. Xu, *Opt. Express*, 2016, **24**, 2830–2835.
- 15 Z. Y. Zhang, J. K. Cao, Y. F. Xue, L. L. Tan, S. H. Xu, Z. M. Yang and M. Y. Peng, *J. Am. Ceram. Soc.*, 2018, **101**, 1159–1168.
- 16 Y. F. Xue, J. K. Cao, Z. Y. Zhang, L. P. Wang, S. H. Xu and M. Y. Peng, *J. Am. Ceram. Soc.*, 2018, **101**, 624–633.
- 17 B. Henderson and G. F. Imbusch, *Optical spectroscopy of inorganic solids*, Clarendon, Oxford, 1989.
- 18 S. Kück, *Appl. Phys. B*, 2001, **72**, 515–562.
- 19 Z. W. Pan, Y. Y. Lu and F. Liu, *Nat. Mater.*, 2012, **11**, 58–63.
- 20 Z. J. Li, Y. W. Zhang, X. Wu, X. Q. Wu, R. Maudgal, H. W. Zhang and G. Han, *Adv. Sci.*, 2015, **2**, 1500001.
- 21 M. Allix, S. Chenu, E. Véron, T. Poumeyrol, E. A. Kouadri-Boudjelthia, S. Alahraché, F. Porcher, D. Massiot and F. Fayon, *Chem. Mater.*, 2013, **25**, 1600–1606.
- 22 Y. X. Zhuang, J. P. Ueda, S. Tanabe and P. Dorenbos, *J. Mater. Chem. C*, 2014, **2**, 5502–5509.
- 23 Y. Li, S. F. Zhou, Y. Y. Li, K. Sharafudeen, Z. J. Ma, G. P. Dong, M. Y. Peng and J. R. Qiu, *J. Mater. Chem. C*, 2014, **2**, 2657–2663.
- 24 U. Hommerich and K. L. Bray, *Phys. Rev. B*, 1995, **51**, 12133–13141.
- 25 S. T. Lai, B. H. T. Chai, M. Long and R. C. Morris, *IEEE J. Quantum Electron.*, 1986, **22**, 1931–1933.
- 26 A. C. Larson and R. B. Von Dreele, *Los Alamos National laboratory Report LAUR*, 1994, pp. 86–748.
- 27 J. S. Zhong, D. Q. Chen, W. G. Zhao, Y. Zhou, H. Yu, L. F. Chen and Z. G. Jia, *J. Mater. Chem. C*, 2015, **3**, 4500–4510.
- 28 D. A. Keszler and H. Sun, *Acta Crystallogr., Sect. C: Cryst. Struct. Commun.*, 1988, **44**, 1505–1507.
- 29 R. Shannon, *Acta Crystallogr., Sect. A: Cryst. Phys., Diffraction. Gen. Crystallogr.*, 1976, **32**, 751–767.
- 30 Y. Tanabe and S. Sugano, *J. Phys. Soc. Jpn.*, 1954, **9**, 766–779.
- 31 G. Blasse and B. C. Grabmaier, *Luminescent materials*, Springer, Berlin, 1994.
- 32 H. M. Zhu, C. C. Lin, W. Q. Luo, S. T. Shu, Z. G. Liu, Y. S. Liu, J. T. Kong, E. Ma, Y. G. Cao, R. S. Liu and X. Y. Chen, *Nat. Commun.*, 2014, **5**, 5312.
- 33 S. S. Pedro, L. P. Sosman, R. B. Barthem, J. C. G. Tedesco and H. N. Bordallo, *J. Lumin.*, 2013, **134**, 100–106.
- 34 L. G. Van Uitert, *J. Electrochem. Soc.*, 1967, **114**, 1048–1053.
- 35 C. H. Huang, Y. C. Chiu, Y. T. Yeh and T. M. Chen, *ACS Appl. Mater. Interfaces*, 2012, **4**, 6661–6668.
- 36 Z. G. Xia, J. Liu, Q. Li and J. Y. Sun, *Electrochem. Solid-State Lett.*, 2007, **10**, J4–J8.
- 37 J. McKittrick and L. E. Shea-Rohwer, *J. Am. Ceram. Soc.*, 2014, **97**, 1327–1352.
- 38 V. Bachmann, C. Ronda and A. Meijerink, *Chem. Mater.*, 2009, **21**, 2077–2084.
- 39 X. Q. Piao, K. Machida, T. Horikawa, H. Hanzawa, Y. Shimomura and N. Kijima, *Chem. Mater.*, 2007, **19**, 4592–4599.
- 40 W. Z. Lv, Y. C. Jia, Q. Zhao, M. M. Jiao, B. Q. Shao, W. Lü and H. P. You, *Adv. Opt. Mater.*, 2014, **2**, 183–188.

